

# CHANDRA HIGH-RESOLUTION SPECTROSCOPY OF THE CIRCUMNUCLEAR MATTER IN THE BROAD-LINE RADIO GALAXY 3C 445

J. N. REEVES<sup>1,4</sup>, J. GOFFORD<sup>1</sup>, V. BRAITO<sup>2</sup>, AND R. SAMBRUNA<sup>3</sup>

<sup>1</sup> Astrophysics Group, School of Physical & Geographical Sciences, Keele University, Keele ST5 5BG, UK; [jnr@astro.keele.ac.uk](mailto:jnr@astro.keele.ac.uk)

<sup>2</sup> Department of Physics & Astronomy, University of Leicester, University Road, Leicester LE1 7RH, UK

<sup>3</sup> Code 662, NASA Goddard Space Flight Center, Greenbelt, MD 20771, USA

Received 2010 June 17; accepted 2010 October 8; published 2010 November 19

## ABSTRACT

We present evidence for X-ray line emitting and absorbing gas in the nucleus of the broad-line radio galaxy 3C 445. A 200 ks *Chandra* Low Energy Transmission Grating observation of 3C 445 reveals the presence of several highly ionized emission lines in the soft X-ray spectrum, primarily from the He- and H-like ions of O, Ne, Mg, and Si. Radiative recombination emission is detected from O VII and O VIII, indicating that the emitting gas is photoionized. The He-like emission appears to be resolved into forbidden and intercombination line components, which implies a high density of  $>10^{10} \text{ cm}^{-3}$ , while the oxygen lines are velocity broadened with a mean width of  $\sim 2600 \text{ km s}^{-1}$  (FWHM). The density and widths of the ionized lines indicate an origin of the gas on sub-parsec scales in the broad-line region. The X-ray continuum of 3C 445 is heavily obscured either by a partial coverer or by a photoionized absorber of column density  $N_{\text{H}} = 2 \times 10^{23} \text{ cm}^{-2}$  and ionization parameter  $\log \xi = 1.4 \text{ erg cm s}^{-1}$ . However, the view of the X-ray line emission is unobscured, which requires the absorber to be located at radii well within any parsec-scale molecular torus. Instead we suggest that the X-ray absorber in 3C 445 may be associated with an outflowing but clumpy accretion disk wind, with an observed outflow velocity of  $\sim 10,000 \text{ km s}^{-1}$ .

**Key words:** galaxies: active – galaxies: individual (3C 445) – X-rays: galaxies

*Online-only material:* color figures

## 1. INTRODUCTION

The X-ray emission from active galactic nuclei (AGNs) is a powerful tool to investigate the structure and physical conditions of the matter in the proximity of the central supermassive black hole. Sensitive X-ray spectroscopy has been very successful in disentangling the contributions from warm and cold matter in AGNs; e.g., see Turner & Miller (2009) for a review. At soft X-ray energies, more than 50% of nearby Seyfert 1s exhibit complex intrinsic absorption and/or emission lines suggesting the presence of photoionized gas (Crenshaw et al. 2003; Blustin et al. 2005; McKernan et al. 2007), which may contain a significant fraction of the accreting mass. This is observed in the form of X-ray absorption in type-1 AGNs, otherwise known as “warm absorbers,” which have typical outflow velocities in the UV and X-ray band of  $100\text{--}1000 \text{ km s}^{-1}$  (Crenshaw et al. 2003). The same absorbing gas is thought to be responsible for the soft X-ray emission lines observed in type-2 sources (Guainazzi & Bianchi 2007; Kinkhabwala et al. 2002; Turner et al. 1997), which may be associated with parsec-scale gas, photoionized by the inner central engine. Furthermore, in a handful of radio-quiet AGNs, blueshifted absorption features have been observed with higher velocity shifts, through detections of resonance absorption lines in the iron *K* band, indicating an outflow from the nucleus with quasi-relativistic velocities,  $v/c \sim 0.1$  (e.g., see Tombesi et al. 2010a and references therein).

Until very recently, the general consensus from the X-ray spectra of radio-loud AGNs was that, unlike their radio-quiet cousins, they contained little or no ionized gas in their nuclei. Thus, there appeared to be no evidence for ionized emitting or absorbing gas in the soft X-ray spectra of broad-line radio

galaxies (BLRGs). For instance, a 120 ks *Suzaku* observation of 3C 120 showed a featureless continuum at soft X-rays, attributed to the radio jet (Kataoka et al. 2007), while a featureless soft X-ray continuum was observed in 3C 390.3 (Sambruna et al. 2009).

Recent sensitive observations with *Chandra*, *XMM-Newton*, and *Suzaku* are subverting this view. Lines in emission and absorption have been detected at soft X-rays in type-1 (broad-line, BLRGs) and type-2 (narrow-line, NLRGs) radio galaxies, indicating large gas column densities of  $N_{\text{H}} = 10^{21}\text{--}10^{23} \text{ cm}^{-2}$  and a range of ionization parameters,  $\log \xi \sim 1\text{--}5 \text{ erg cm s}^{-1}$  (Sambruna et al. 2007; Grandi et al. 2007; Piconcelli et al. 2008; Torresi et al. 2009, 2010; Reeves et al. 2009; Tombesi et al. 2010b). Ionized soft X-ray emission lines have so far been detected in the BLRG 3C 445 (Sambruna et al. 2007; Grandi et al. 2007) and in the NLRGs 3C 234 (Piconcelli et al. 2008) and 3C 33 (Torresi et al. 2009). Photoionized absorption lines, consistent with gas outflowing on parsec scales with velocities of hundreds of  $\text{km s}^{-1}$ , were detected for the first time with grating resolution X-ray spectra in the BLRG 3C 382, with *Chandra*/HETG (Reeves et al. 2009) and independently with *XMM-Newton*/RGS (Reflection Grating Spectrometer) (Torresi et al. 2010). Interestingly, *Suzaku* observations of BLRGs have also uncovered evidence at higher energies, at 7–9 keV in the iron *K* band, for fast outflowing gas with velocities  $v_{\text{out}} \sim 0.04\text{--}0.15c$ , carrying substantial masses and kinetic powers similar to the radio jets (Tombesi et al. 2010b). Thus, there appears to be substantial ionized gas in the nuclei of radio-loud AGNs, and this gas may be an energetically important component that needs to be accounted for in models for accretion and jet formation.

Indeed, there are reasons to expect the presence of such a medium in BLRGs and other radio-loud AGNs. For example, centrifugally driven winds, lifting matter off the disk’s surface

<sup>4</sup> Also at: CSST, University of Maryland Baltimore County, 1000 Hilltop Circle, Baltimore, MD 21250, USA.

and channelling it down the magnetic field, are a proposed scenario for the origin of relativistic jets (Blandford & Payne 1982); at favorable orientations, these winds lead to observable discrete absorption/emission features at soft X-rays (Königl & Kartje 1994). Jet formation models predict that the relativistically moving plasma should be enveloped in a sub-relativistic wind (McKinney 2006), with velocities  $\lesssim 0.1c$ . Unification models for radio-loud sources also postulate the presence of a warm, scattering gas to explain type-2 sources (Antonucci 1993; Urry & Padovani 1995).

### 1.1. The Broad-line Radio Galaxy 3C 445

3C 445 is a bright, nearby ( $z = 0.0562$ ; Hewitt & Burbidge 1991; Eracleous & Halpern 2004), and luminous ( $L_{\text{bol}} \sim 10^{45} \text{ erg s}^{-1}$ ; Marchesini et al. 2004) radio galaxy with an FR II morphology (Kronberg et al. 1986). 3C 445 appears lobe rather than core dominated (Morganti et al. 1993) and is likely to be highly inclined with respect to the radio-jet axis, with an inclination angle of  $\sim 60^\circ$ – $70^\circ$  (Eracleous & Halpern 1998; Sambruna et al. 2007). Based on its optical spectra it is classed as a BLRG, due to the presence of strong broad permitted lines in unpolarized light (Osterbrock et al. 1976; Crenshaw et al. 1988; Eracleous & Halpern 1994; Corbett et al. 1998). From its rather large Balmer decrement, the line-of-sight reddening toward 3C 445 is  $E_{B-V} \sim 1$ , which for a Galactic dust-to-gas ratio suggests an absorbing column density of  $N_{\text{H}} \sim 5 \times 10^{21} \text{ cm}^{-2}$ , an order of magnitude higher than the Galactic line-of-sight column (Dickey & Lockman 1990).

3C 445 is also a bright source in the X-ray band, having previously been detected by *EXOSAT* (Turner & Pounds 1989), *Ginga* (Pounds 1990), *ASCA* (Sambruna et al. 1998), and is also detected in the hard X-ray band (above 10 keV), with *BepoSAX* (Grandi et al. 2006), *Swift*/BAT (Burst Alert Telescope; Tueller et al. 2010), and most recently with *Suzaku* (V. Braito et al. 2010, in preparation). Past observations with *EXOSAT*, *Ginga*, and *ASCA* all indicated an absorbed X-ray spectrum, with a column density of  $N_{\text{H}} \sim 10^{23} \text{ cm}^{-2}$ , far in excess of the column density expected from the amount of reddening in the optical spectra of 3C 445. A more recent short (15 ks) *XMM-Newton* observation of 3C 445 confirmed the absorbed nature of its X-ray emission, with the absorber either partially covering the AGN or consisting of partially ionized material (Sambruna et al. 2007; Grandi et al. 2007).

Most interestingly, the *XMM-Newton* observations suggested the presence of multiple highly ionized soft X-ray emission lines (Sambruna et al. 2007; Grandi et al. 2007), primarily from O, Mg, and Si, with a spectrum somewhat reminiscent of those of Seyfert 2 galaxies (Guainazzi & Bianchi 2007). Given the relatively low exposure and lower resolution of the *XMM-Newton* EPIC-pn data below 2 keV, it was impossible to deduce the physical properties or location of the emitting gas, which was constrained to lie within  $<5 \text{ kpc}$  of the nucleus in 3C 445 (Sambruna et al. 2007). A tentative detection of the O VII and O VIII emission lines was made in the *XMM-Newton* RGS observations (Grandi et al. 2007); however, the short exposure precluded a more detailed analysis of the soft X-ray line emitting gas.

In this paper, we present direct evidence for the photoionized circumnuclear gas around the nucleus of 3C 445 from high-resolution spectroscopy with the *Chandra* Low Energy Transmission Grating (LETG; Brinkman et al. 2000). In this much deeper 200 ks exposure, we resolve multiple emission lines in the soft X-ray band from the high-resolution LETG

data. The higher quality of the data allows us to determine the properties and location of the emitting matter, which as we will subsequently show is most likely to be emission from highly ionized gas associated with the broad-line region (BLR) clouds in 3C 445. The *Chandra* LETG spectrum also allows an accurate measurement of the properties of the absorbing gas toward 3C 445, which appears to be outflowing with respect to the rest frame of 3C 445. A subsequent paper (V. Braito et al. 2010, in preparation) will discuss in detail the broadband X-ray spectrum of 3C 445 observed with *Suzaku* and *Swift*.

The organization of this paper is as follows. In Section 2, we describe the *Chandra* data reduction and analysis, in Section 3 the results of the spectral analysis, and in Section 4 the photoionization modeling of the spectrum. Discussion and conclusions follow in Sections 5 and 6. Throughout this paper, a concordance cosmology with  $H_0 = 71 \text{ km s}^{-1} \text{ Mpc}^{-1}$ ,  $\Omega_{\Lambda} = 0.73$ , and  $\Omega_m = 0.27$  (Spergel et al. 2003) is adopted. Errors are quoted to 90% confidence for one parameter of interest (i.e.,  $\Delta\chi^2$  or  $\Delta C = 2.71$ ). All the spectral parameters in subsequent sections are quoted in the rest frame of 3C 445 ( $z = 0.0562$ ) unless otherwise stated.

## 2. THE CHANDRA LETG OBSERVATIONS

*Chandra* observed 3C 445 with the LETG for a net exposure of 198 ks between 2009 September 25 and October 3, with the ACIS-S detector in the focal plane. The zeroth-order image of 3C 445 at the aim point of ACIS-S appears unresolved. No significant source variability was found during the observations, so the time-averaged data were used. The  $\pm 1$  order spectra were summed for the LETG, respectively, along with their response files. The resultant summed (background subtracted) first-order count rate for the LETG is  $0.0318 \pm 0.0004 \text{ counts s}^{-1}$  over the energy range 0.5–9.0 keV.

## 3. THE SOFT X-RAY SPECTRUM OF 3C 445

### 3.1. Initial Continuum Modeling

Initially, in order to parameterize the LETG spectrum of 3C 445 with simple continuum models, we binned the spectra to a minimum of 10 source counts  $\text{bin}^{-1}$  and applied the  $\chi^2$  statistic. The continuum of the LETG spectrum from 3C 445 can be very crudely parameterized by a broken-power-law model, as is shown in Figure 1. The spectrum at higher energies, above a break energy of  $\sim 1.4 \text{ keV}$  ( $\sim 9 \text{ \AA}$ ), is very hard, rising with energy (decreasing wavelength) with a photon index of  $\Gamma = -0.64 \pm 0.03$ . Below the break, the X-ray spectrum is softer, with  $\Gamma = 1.73 \pm 0.21$ . This initial parameterization of the data provided a poor fit (with  $\chi^2/\text{dof} = 568.5/181$ , null hypothesis probability  $P = 1.3 \times 10^{-41}$ , where dof is the number of degrees of freedom in the fit). At soft X-ray energies, there is statistically significant scatter around the continuum due to the presence of likely emission lines, while at higher energies, residuals are present in the data, most notably emission and absorption in the iron *K* band between 6 and 8 keV ( $\sim 2 \text{ \AA}$ ). The observed flux of 3C 445 from 0.5 to 9 keV is  $8.84 \times 10^{-12} \text{ erg cm}^{-2} \text{ s}^{-1}$ .

In order to provide a more physical representation of the continuum, we fit the spectrum with a photoelectric absorption model of the form  $F(E) = \text{wabs} \times (\text{zwabs} \times \text{pow1} + \text{pow2})$ , where pow1 represents an absorbed power law, pow2 the unabsorbed power-law continuum (i.e., absorbed only by the Galactic column density), wabs is the local Galactic line-of-sight absorber (where  $N_{\text{H,Gal}} = 4.6 \times 10^{20} \text{ cm}^{-2}$  for 3C 445;

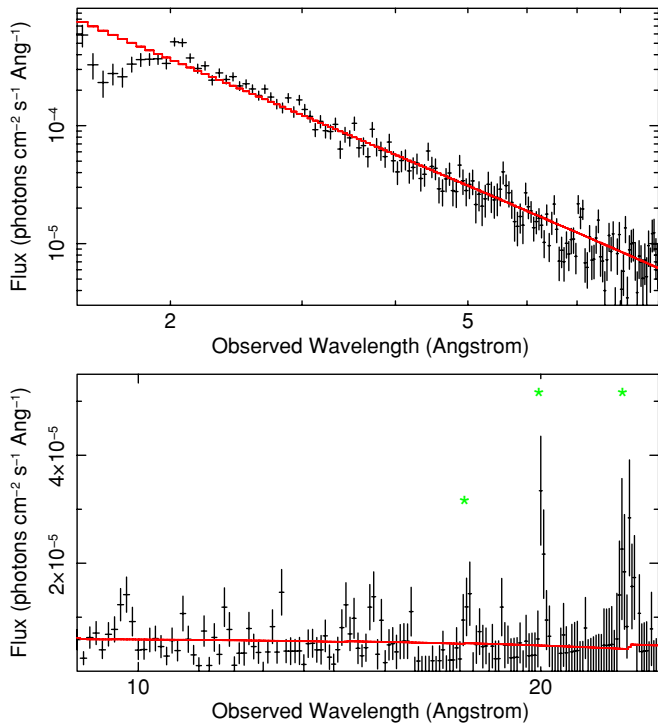


**Figure 1.** *Chandra* LETG spectrum of 3C 445, showing the hard X-ray (top) and soft X-ray regions (bottom) against observed-frame wavelength. The fluxed spectrum (black crosses) is plotted against a broken power-law continuum (solid line) for reference. The spectrum shortward of 9 Å ( $>1.4$  keV) is very hard, rising with energy (decreasing wavelength) with a photon index of  $\Gamma = -0.64$ , indicative of a highly absorbed continuum. Note the emission and absorption present at iron *K*. In the soft X-ray band, several emission lines appear to be present. The star symbols denote the expected positions of (from right to left) the O VII He- $\alpha$  (forbidden or intercombination), O VIII Ly $\alpha$  and the O VII radiative recombination emission.

(A color version of this figure is available in the online journal.)

Dickey & Lockman 1990), and *zwabs* is the intrinsic absorber of column density  $N_{\text{H}}$  toward 3C 445, fitted in the rest frame of the radio galaxy ( $z = 0.0562$ ). Solar abundances are assumed (Anders & Grevesse 1989), while the neutral absorber uses cross sections of Morrison & McCammon (1983).

The photon indices of the two power-law components in the above model are assumed to be the same; however, their respective normalizations are allowed to differ. Thus, the unabsorbed power law may represent soft X-ray emission which is Thomson scattered into our line of sight, while the absorbed power law represents the intrinsic hard X-ray emission from an accretion disk corona. An intrinsic column density of  $N_{\text{H}} = (12.3 \pm 1.3) \times 10^{22} \text{ cm}^{-2}$  is required, while the derived photon index is still rather flat ( $\Gamma = 0.78 \pm 0.13$ ) compared to the typical values in radio-loud AGNs (e.g., Sambruna et al. 1999; Reeves & Turner 2000).

The model is a statistically poor representation of the data ( $\chi^2/\text{dof} = 421.1/181$ ,  $P = 3.2 \times 10^{-21}$ ); in the soft X-ray band narrow emission-like residuals are present, while at high energies significant spectral curvature is present, as well as emission and absorption in the iron *K* band. The spectral curvature and very hard photon index may indicate that a more complex absorber is present, which was found to be the case in the *XMM-Newton* spectrum of 3C 445 (Sambruna et al. 2007).

Thus, instead, the spectrum was parameterized by a dual absorber of the form  $F(E) = \text{wabs} \times (\text{zwabs} \times \text{zpcfabs} \times \text{pow1} + \text{pow2})$ , where *zpcfabs* is a photoelectric absorber which partially

covers our line of sight toward the source. Thus, some fraction ( $f_{\text{cov}}$ ) of the primary hard X-ray power law (*pow1*) is absorbed by the partial coverer, while the remaining fraction ( $1 - f_{\text{cov}}$ ) is absorbed only by the fully covering absorber (*zwabs*). The scattered soft X-ray power-law continuum is absorbed only by the Galactic column, as previously described. This dual absorber provides a good description of the continuum, especially above 2 keV where the spectral curvature is no longer present in the data/model residuals. The column density of the partial coverer is then  $N_{\text{H,pcov}} = (3.6 \pm 0.5) \times 10^{23} \text{ cm}^{-2}$ , with a covering fraction of  $f_{\text{cov}} = 0.86 \pm 0.03$ , while the fully covering absorber has a lower column of  $N_{\text{H}} = (5.7 \pm 0.6) \times 10^{22} \text{ cm}^{-2}$ . The ratio of the unabsorbed (scattered) to absorbed power-law continuum is lower,  $f_{\text{scatt}} \sim 0.01$ , consistent with what is seen in other absorbed AGNs (e.g., Turner et al. 1997). The power-law photon index is now much steeper, with  $\Gamma = 1.84 \pm 0.04$ .

Nonetheless, the fit statistic is still poor ( $\chi^2/\text{dof} = 314.7/179$ ,  $P = 1.6 \times 10^{-9}$ ), with several emission lines apparent below 2 keV (e.g., in the O VII–VIII band) and at Fe *K*. Indeed evidence for soft X-ray line emission has been previously suggested by the *XMM-Newton* spectra of this source (Sambruna et al. 2007; Grandi et al. 2007). Below we give a detailed description of these emission lines, utilizing the full spectral resolution of the *Chandra*/LETG. We return in Section 4 to discuss more physical models for both the absorber and emitter, using the photoionization code *XSTAR* (Kallman et al. 2004).

### 3.2. The Soft X-ray Emission Line Spectrum of 3C 445

To analyze the emission lines in detail, the LETG spectra were binned more finely to sample the resolution of the detector, at approximately the FWHM spectral resolution (e.g.,  $\Delta\lambda = 0.05 \text{ Å}$  bins). Thus, the spectral resolution is  $E/\Delta E \sim 500$  (or  $600 \text{ km s}^{-1}$  FWHM) at 0.5 keV. For the fits, the *C*-statistic was adopted (Cash 1979) rather than  $\chi^2$ , as there are fewer than 10 counts in some of the resolution bins.

The emission lines were modeled with Gaussian profiles and the best-fit partial covering continuum model was adopted from above, allowing the continuum and absorption parameters to vary. Table 1 lists the detected lines with their observed and inferred properties, and their significance as per the *C*-statistic. Figures 2 and 3 show the portions of the LETG spectrum containing the strongest lines, with the model overlaid. Overall the fit statistic improves considerably upon the addition of the emission lines to the continuum model, i.e., from  $C/\text{dof} = 720.2/444$  without emission lines (rejected at  $>99.99\%$  confidence) to  $C/\text{dof} = 448.3/425$  upon adding the emission lines (rejected at only 85% confidence).

Indeed the majority of the individual emission lines in Table 1 are detected at high confidence, corresponding to  $\Delta C > 14$ , or  $>99.9\%$  significance for two parameters of interest (lines detected with a lower level of confidence are noted). For instance, the O VII He- $\alpha$  and O VIII Ly $\alpha$  lines are detected with  $\Delta C > 50$ . The strongest emission lines correspond to the He-like (He- $\alpha$ ) and H-like (Ly $\alpha$ ) transitions from O VII–VIII, Ne IX–X, Mg XI–XII, and Si XIII–XIV. Fluorescence lines may also be present from Si *K* $\alpha$  and Fe *K* $\alpha$  at 2.3 and 6.4 keV, respectively, which may originate from reflection off Compton-thick matter (see Section 4.1). Most of the rest-frame energies of the emission lines are close to their expected lab values<sup>5</sup> (see Table 1), implying that the outflow velocity of the emitting gas is within  $<1000 \text{ km s}^{-1}$ .

<sup>5</sup> Line energies and atomic data are adopted from <http://physics.nist.gov>.

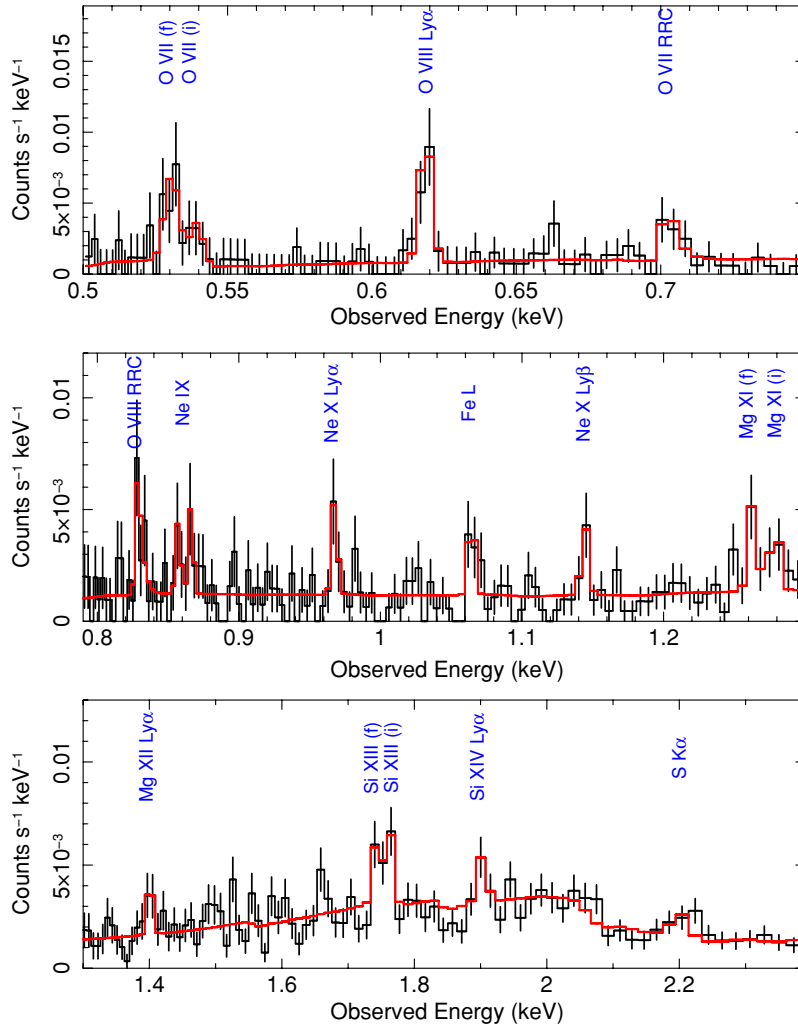


**Figure 2.** *Chandra* LETG spectra of 3C 445 showing several soft X-ray emission lines from O, Ne, Mg, Si, and Fe L. The solid line represents the best-fit absorbed continuum model with Gaussian emission lines, as described in Section 3.2 and Tables 1 and 2.

(A color version of this figure is available in the online journal.)

### 3.2.1. Radiative Recombination Emission

In addition, radiative recombination continua (RRCs) are detected from both O VII and O VIII at high ( $>99.9\%$ ) significance. For instance, the emission line detected at  $700.8 \pm 1.3$  eV ( $17.71$  Å) corresponds to a rest-frame energy of  $740.1 \pm 1.4$  eV ( $16.77$  Å), which is consistent with the expected energy ( $739.3$  eV) of the O VII RRC. These have been modeled with emission from recombination edges, of variable width dependent on temperature  $kT$ , rather than as Gaussians. Note that both RRCs are resolved with a width of  $kT \sim 3$  eV (see Table 1), which implies a temperature of  $\sim 3 \times 10^4$  K for the emitting gas. This suggests an origin in a photoionized rather than collisionally ionized (thermal) plasma, as the temperature would need to be closer to  $\sim 10^7$  K to produce substantial soft X-ray line emission from collisionally ionized gas.

### 3.2.2. The He-like Line Emission

The He-like lines all appear to be resolved when modeled with a single Gaussian profile (see Table 1). Thus, the He-like emission may contain a blend of lines from the forbidden (f), intercombination (i), and resonance (r) transitions. Indeed the rest energy of the He-like lines is intermediate between

the expected resonance and intercombination transitions: e.g., O VII at 565 eV is intermediate between 561 eV (f) and 569 eV (i). Thus, the He-like emission was fitted by a blend of two separate emission lines and the results are reported in Table 2. This provides an acceptable parameterization of the spectrum ( $C/\text{dof} = 445.3/423$ ). The rest energies of the O VII and Ne IX lines are all consistent (within an eV) of the expected energies of the forbidden and intercombination transitions. Figures 2 and 3 show the spectrum fitted with this line model.

In all the cases, the strengths of the forbidden and intercombination emission are approximately equal (see Table 2), implying a high-density plasma, i.e.,  $n_e > 10^{10} \text{ cm}^{-3}$  (Porquet & Dubau 2000). The  $R$  ratio quantifies the ratio of the forbidden to intercombination line strengths; i.e.,  $R = z/(x + y)$ , where  $z$  is the forbidden line and  $x+y$  represents the sum of the intercombination emission. In the 3C 445 spectrum, the best constraints on  $R$  arise from the O VII triplet. Allowing the ratio of the forbidden and intercombination lines to vary results in a value of  $R = 0.9^{+1.1}_{-0.3}$  (at 90% confidence), which implies an electron density in the region of  $n_e = 10^{10}$ – $10^{11} \text{ cm}^{-3}$  (e.g., Figure 8 of Porquet & Dubau 2000). This suggests that the emission originates from matter closer in than the narrow-line region (NLR), a point we discuss further in Section 5.



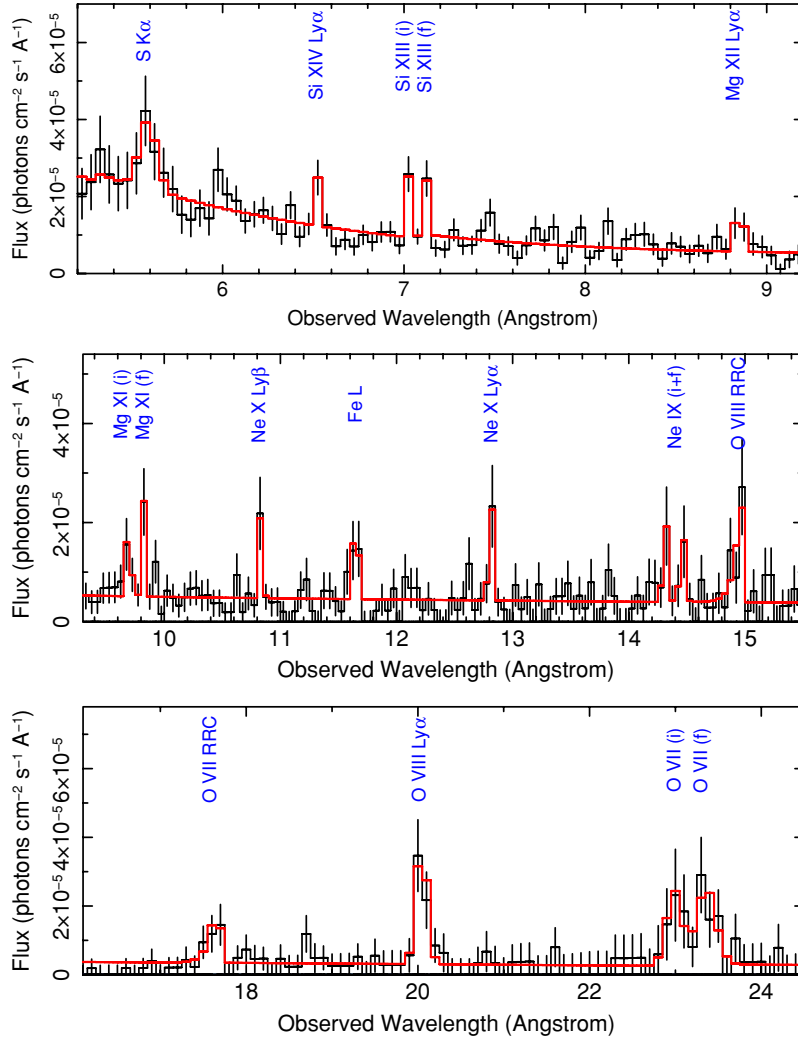


**Figure 3.** Fluxed LETG spectrum, plotted against observed-frame wavelength (in Å). The solid line shows the same line model as plotted in Figure 2. (A color version of this figure is available in the online journal.)

### 3.2.3. Line Widths

The velocity widths of the O VII and O VIII emission lines were also determined. The O VIII Ly $\alpha$  line is resolved with a width of  $\sigma = 2.0^{+1.1}_{-0.9}$  eV (see Table 1), corresponding to a FWHM width of  $2100^{+1100}_{-950}$  km s $^{-1}$ ; the fit statistic worsens by  $\Delta C = 12$  if the line width is set to zero. Note that the separation of the O VIII Lyman- $\alpha$  doublet has a negligible effect on the line width. Upon modeling the He-like triplet emission using two separate Gaussian lines to represent the forbidden and intercombination emission, the O VII He- $\alpha$  line width was also determined, giving  $\sigma = 2.4^{+2.8}_{-0.8}$  eV (see Table 1), which corresponds to a FWHM width of  $3000^{+3400}_{-980}$  km s $^{-1}$ . Note that the line widths of the forbidden and intercombination lines were assumed to be equal to each other in the model. The fit statistic also worsened significantly ( $\Delta C = +31$ ) when the velocity width of the O VII lines was fixed to zero. The lines from higher-Z ions were not resolved, as the LETG spectral resolution worsens with increasing energy; however, the upper limits to their widths are consistent with the values from the oxygen lines (see Table 1 for the H-like ions and Table 2 for the He-like ions).

In order to derive the most accurate determination of the line velocity width, we assumed that the widths of the three strongest lines from O VII(f), O VII(i), and O VIII Ly $\alpha$  were iden-

tical and tied these values in the resulting model. The resolution of the LETG is also at its highest in the O band. This yielded a best-fit velocity width of  $\sigma = 1120^{+430}_{-270}$  km s $^{-1}$  (or  $\sigma = 2.1^{+0.8}_{-0.5}$  eV at 561 eV), corresponding to a FWHM width of  $v_{\text{FWHM}} = 2600^{+1000}_{-600}$  km s $^{-1}$ . A contour plot showing the measurement of the FWHM velocity width of the oxygen lines is shown in Figure 4, which shows that a velocity width of zero is excluded at >99.99% confidence (with  $\Delta C = +42$ ).

## 4. PHOTOIONIZATION MODELING

As discussed above, the presence of strong RRCs may suggest that the soft X-ray line emission originates from a photoionized rather than collisionally ionized plasma (Kinkhabwala et al. 2002). To test this, the spectrum was fitted with a collisional model, such as the MEKAL (Kaastra & Mewe 1993) or APEC (Smith et al. 2001) codes. We used the same continuum parameterization as before, except the ionized emission lines modeled by Gaussians are replaced by emission from a collisionally ionized APEC model. A single-temperature collisional model of temperature  $kT = 0.24 \pm 0.04$  keV does not provide an acceptable fit to the data ( $C/\text{dof} = 610.5/456$ ) and the model is rejected at >99.99% confidence. Figure 5 (upper panel) shows the spectrum fitted with the APEC model in the oxygen band:

**Table 1**  
Summary of LETG Emission Line Parameters

$E_{\text{rest}}$ (eV)	$\lambda_{\text{rest}}$ (Å)	Line Flux <sup>a</sup>	$\sigma$ or $kT$ (eV) <sup>b</sup>	EW (eV)	$\Delta C^c$	Line ID	$E_{\text{lab}}^d$ (eV)
$564.6 \pm 2.6$	$21.98 \pm 0.10$	$18.8^{+7.6}_{-6.2}$	$6.3^{+2.8}_{-1.8}$	$105^{+42}_{-35}$	55.0	O VII He $\alpha$	561.1(f)
$653.4 \pm 1.0$	$18.99 \pm 0.03$	$8.3^{+4.0}_{-3.0}$	$2.0^{+1.2}_{-0.9}$	$62^{+29}_{-22}$	54.4	O VIII Ly $\alpha$	653.7
$740.2 \pm 1.4$	$16.76 \pm 0.03$	$3.2^{+2.4}_{-1.7}$	$3.5^{+3.6}_{-1.9}$	$31^{+22}_{-15}$	18.8	O VII RRC	739.3
$873.8 \pm 1.4$	$14.20 \pm 0.02$	$2.2^{+1.5}_{-1.1}$	$3.0^{+4.0}_{-2.0}$	$21^{+12}_{-10}$	19.6	O VIII RRC	871.4
$913 \pm 5$	$13.59 \pm 0.07$	$2.6^{+1.6}_{-1.3}$	$7.2^{+4.0}_{-2.0}$	$25^{+15}_{-12}$	14.6	Ne IX He $\alpha$	905.1(f)
$1022^{+1}_{-2}$	$12.14^{+0.01}_{-0.02}$	$1.3^{+1.0}_{-0.8}$	$<4.0$	$19^{+15}_{-12}$	14.2	Ne X Ly $\alpha$	1022
$1124 \pm 2$	$11.04 \pm 0.02$	$1.2^{+0.9}_{-0.7}$	...	$20^{+14}_{-12}$	11.8 <sup>e</sup>	Fe XXIII	1125
$1209^{+3}_{-2}$	$10.26^{+0.03}_{-0.02}$	$0.9^{+0.8}_{-0.6}$	...	$18^{+16}_{-12}$	10.7 <sup>e</sup>	Ne X Ly $\beta$	1211
$1341 \pm 7$	$9.25 \pm 0.05$	$2.6^{+1.2}_{-1.0}$	$14.5^{+9.0}_{-5.0}$	$59^{+27}_{-23}$	26.1	Mg XI He $\alpha$	1331(f)
$1480 \pm 3$	$8.38 \pm 0.02$	$0.8^{+0.6}_{-0.5}$	$<21$	$21^{+16}_{-13}$	10.2 <sup>e</sup>	Mg XII Ly $\alpha$	1472
$1853 \pm 6$	$6.97 \pm 0.02$	$1.4^{+0.6}_{-0.5}$	$10.5^{+5.5}_{-4.0}$	$32^{+14}_{-11}$	23.7	Si XIII He $\alpha$	1839(f)
$2010^{+6}_{-10}$	$6.17^{+0.02}_{-0.03}$	$0.7^{+0.5}_{-0.4}$	$<13$	$13^{+16}_{-9}$	9.5 <sup>e</sup>	Si XIV Ly $\alpha$	2006
$2343^{+16}_{-9}$	$5.30^{+0.04}_{-0.02}$	$2.5^{+1.5}_{-1.3}$	$<38$	$43^{+25}_{-22}$	11.5 <sup>e</sup>	S I K $\alpha$	2307
$6364^{+40}_{-43}$	$1.95 \pm 0.01$	$22.9^{+6.6}_{-6.1}$	$<145$	$191^{+55}_{-51}$	55.6	Fe I K $\alpha$	

**Notes.**

<sup>a</sup> Measured flux in units of  $10^{-6}$  photons  $\text{cm}^{-2} \text{s}^{-1}$ .

<sup>b</sup>  $1\sigma$  width of Gaussian line or temperature of RRCs (in eV). If only an upper limit to the width is determined, the width has been fixed at  $\sigma = 1$  eV in the model.

<sup>c</sup> Improvement in  $C$  to fit after adding emission line component.

<sup>d</sup> Expected line energy of transition taken from <http://physics.nist.gov>.

<sup>e</sup> Line detection significance at lower than 99.9% confidence.

**Table 2**  
Summary of He-like Triplets

$E_{\text{rest}}$ (eV)	$\lambda_{\text{rest}}$ (Å)	Line Flux <sup>a</sup>	$\sigma$ (eV) <sup>b</sup>	EW (eV)	$\Delta C^c$	Line ID <sup>d</sup>	$E_{\text{lab}}$ (eV)
$560.7 \pm 1.4$	$22.13 \pm 0.06$	$8.6^{+4.7}_{-3.7}$	$2.4^{+2.8}_{-0.8}$	$27^{+23}_{-12}$	35.2	O VII(f)	561.1
$569.5 \pm 1.6$	$21.79 \pm 0.06$	$9.2^{+7.2}_{-4.1}$	...	$21^{+20}_{-11}$	16.0	O VII(i)	568.7
$905.4 \pm 2.3$	$13.70 \pm 0.03$	$1.0^{+1.0}_{-0.7}$	$<5$	$8^{+10}_{-6}$	6.5 <sup>e</sup>	Ne IX(f)	905.1
$914.8 \pm 2.0$	$13.56 \pm 0.03$	$1.2^{+1.0}_{-0.7}$	...	$13^{+21}_{-10}$	9.0 <sup>e</sup>	Ne IX(i)	914.8
$1334^{+2}_{-3}$	$9.30^{+0.01}_{-0.02}$	$1.1^{+0.7}_{-0.5}$	$<21$	$19^{+12}_{-9}$	16.4	Mg XI(f)	1331
$1351^{+6}_{-3}$	$9.18^{+0.04}_{-0.02}$	$0.8^{+0.7}_{-0.5}$	...	$15^{+13}_{-9}$	9.7	Mg XI(i or r)	1343 or 1352
$1842^{+4}_{-5}$	$6.74 \pm 0.02$	$0.8^{+0.5}_{-0.4}$	$<6$	$16^{+10}_{-8}$	12.0	Si XIII(f)	1839
$1861 \pm 3$	$6.67 \pm 0.01$	$1.1^{+0.5}_{-0.4}$	...	$25^{+11}_{-9}$	20.0	Si XIII(i or r)	1854 or 1865

**Notes.**

<sup>a</sup> Measured flux in units of  $10^{-6}$  photons  $\text{cm}^{-2} \text{s}^{-1}$ .

<sup>b</sup> Line widths, assuming the widths of the forbidden and intercombination lines are set to be equal for any single ion.

<sup>c</sup> Improvement in  $C$  to fit after adding emission line component.

<sup>d</sup> Forbidden, intercombination, and resonance lines denoted by (f), (i), and (r). Expected lab-frame line energies in parentheses in eV.

<sup>e</sup> Line detection significance at lower than 99% confidence.

the model fails to account for the O VII triplet (the resonance line is the strongest predicted line, which is not present in the actual data), and does not fit the recombination emission. We also investigated whether a multiple-temperature collisionally ionized model or a model with non-solar abundances further improved the fit, but this was not the case. Thus, the data appear to exclude a collisionally ionized plasma for the origin of the soft X-ray emission lines.

#### 4.1. The Soft X-ray Emitter

Thus, instead we used a grid of emission models calculated by the photoionization code XSTAR v2.1 (Kallman & McCray 1982; Kallman et al. 2004) to derive the parameters of the emitter, assuming the baseline continuum described above. Solar abundances are assumed throughout (Grevesse & Sauval

1998). A turbulent velocity of  $500 \text{ km s}^{-1}$  has been used for the emission model.<sup>6</sup> We assumed an initial column density of  $N_{\text{H}} = 10^{22} \text{ cm}^{-2}$  for the emitter as this cannot be fitted directly to the data, unlike for an absorption model, as the  $N_{\text{H}}$  and total covering factor of the emitter are largely degenerate upon each other. Likely values for both the column and covering of the emitter will be discussed further in Section 5.1.2.

The overall model fitted to the data is in the same form as the partial covering model described in Section 3.1, i.e.,  $F(E) = \text{wabs} \times (\text{zwabs} \times \text{zpcfabs} \times \text{pow1} + \text{pow2} + \text{xstar}_{\text{em}})$ , where  $\text{xstar}_{\text{em}}$  represents the photoionized emission, which is absorbed only by the Galactic line-of-sight column. The XSTAR model does not include the fluorescent emission from

<sup>6</sup> We have chosen a grid whereby the turbulence velocity best matches the observed velocity width from the Gaussian line fits.

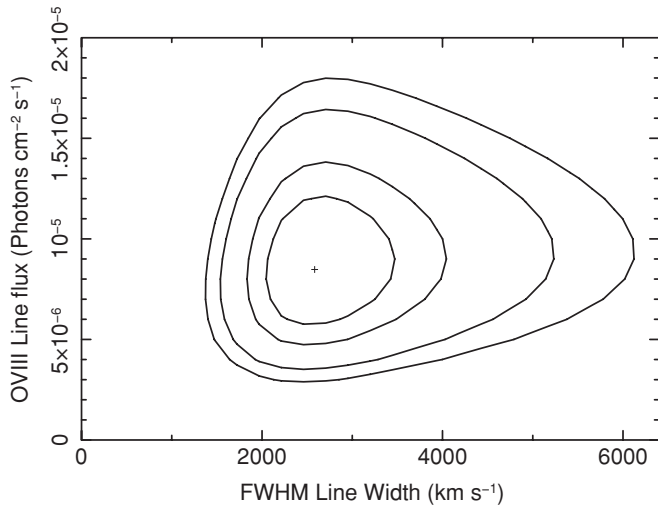


**Figure 4.** FWHM velocity width, fitted jointly to the OVII forbidden/intercombination and OVIII Ly $\alpha$  lines, plotted against OVIII Ly $\alpha$  line flux. The contours represent the 68%, 90%, 99%, and 99.9% confidence levels for two parameters of interest.

S K $\alpha$ , and Fe K $\alpha$ , which have been modeled separately with Gaussian profiles. This provides a significantly better fit to the data than the collisional model; for comparison, Figure 5 (b) shows that the XSTAR model fits the oxygen emission lines well, especially around the OVII triplet and RRC, in contrast to the collisional model. The overall fit statistic is improved to  $C/\text{dof} = 529.1/450$ , which is rejected only at the 90% confidence level. The best-fit parameters of this XSTAR model are listed in Table 3.

The emitter was fitted by two zones of gas of ionization parameter  $\log \xi = 1.8^{+0.1}_{-0.3}$  and  $\log \xi = 3.0 \pm 0.4$ , respectively.<sup>7</sup> Note that a two-zone model gave only a slightly better fit (by  $\Delta C = 9$  for two parameters) than a single-zone model; thus a second higher-ionization emission zone is only required at the  $\sim 99\%$  confidence level. There is also some tentative evidence for super-solar abundances of Mg and Si (all other abundances are consistent with solar), although their values in Table 2 are not well determined.

Note that no outflow velocity is required for the photoionized emitter: indeed a slight redshift is found with  $v_{\text{out}} = +150^{+240}_{-210}$  km s $^{-1}$ , although the data are consistent with zero velocity shift (compared to systemic) for the emitter. Thus, the 90% confidence limit to the emitter outflow velocity is very tightly constrained to within 60 km s $^{-1}$  of the systemic velocity of 3C 445. In comparison, the emitter outflow velocity determined from the XMM-Newton RGS data was  $v_{\text{out}} = -430^{+220}_{-160}$  km s $^{-1}$  (Grandi et al. 2007).

Finally, instead of modeling the Fe K $\alpha$  line with a Gaussian, a model consisting of Compton reflection off an optically thick photoionized slab of gas was tested. The REFLIONX<sup>8</sup> model was used (Ross et al. 1999; Ross & Fabian 2005), assuming solar abundances, with the resulting fit found to be equally good compared to the fit with Gaussian fluorescent lines. The reflector was found to be low ionization, with an upper limit of  $\log \xi < 1.7$ . This is not surprising given that the rest energy of the iron K $\alpha$  emission (see Table 1) is close to the expected

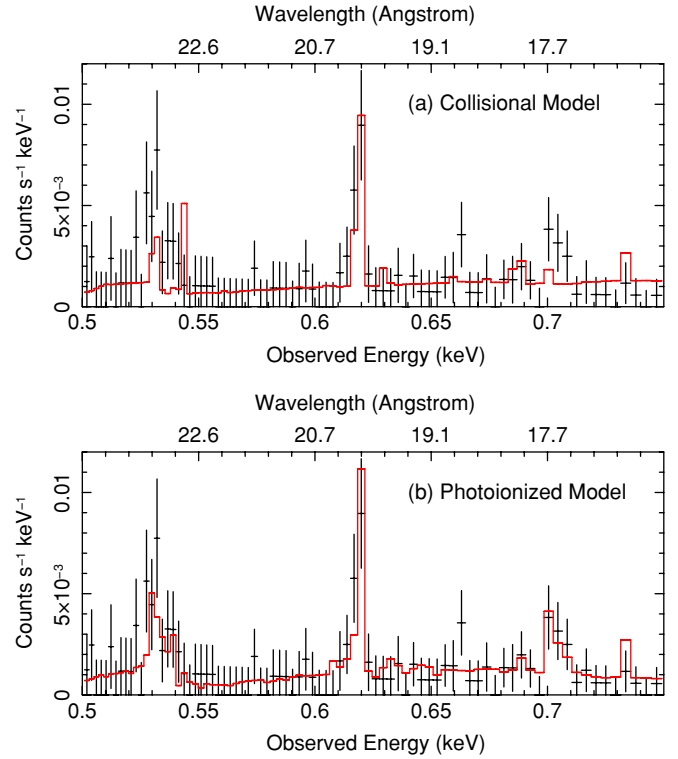


**Figure 5.** Comparison between (a) the collisionally ionized APEC emission model and (b) the photoionized XSTAR emission model in the oxygen band, as discussed in Section 4.

(A color version of this figure is available in the online journal.)

value for neutral or lowly ionized iron (i.e., Fe I–XVII). Note that no velocity broadening is required for the reflection spectrum, which is consistent with the upper limit to the iron K $\alpha$  velocity width of  $\sigma < 145$  eV (or  $\sigma < 6800$  km s $^{-1}$ ). Thus, the reflection spectrum could be consistent with an origin in either the outer accretion disk or a parsec-scale Compton-thick torus. The properties of the reflection component are discussed in more detail in a paper describing the *Suzaku* and *Swift* spectra and the hard X-ray emission above 10 keV (V. Braito et al. 2010, in preparation).

#### 4.2. The X-ray Absorber

The neutral partial covering model provides a good phenomenological description of the absorber in 3C 445, whereby part of the primary X-ray emission is heavily absorbed (by a column of gas of  $N_{\text{H}} > 10^{23}$  cm $^{-2}$ ) along the line of sight. However, this may also approximate a scenario whereby the absorber is partially ionized and thus can be partially transparent to continuum X-rays at soft X-ray energies. Indeed the majority of Seyfert 1 spectra show such a “warm” absorber (e.g., Reynolds 1997; Blustin et al. 2005; McKernan et al. 2007). Here we are more likely to be viewing the nucleus of 3C 445 at higher inclination angles of about 60°–70°, given the likely radio orientation of the system (Eracleous & Halpern 1998; Sambruna et al. 2007). Thus, in 3C 445 we may be viewing the X-ray source directly down an accretion disk wind (Gallagher & Everett 2007) or perhaps through the outer edge of the putative parsec-scale molecular torus (Urry & Padovani 1995).

Initially, as a simple parameterization, the iron K-band absorption was fitted by a simple photoelectric edge model. The energy of the edge was found to be  $E = 7.35 \pm 0.09$  keV in the rest frame of 3C 445, with an optical depth of  $\tau = 1.0 \pm 0.2$ .

<sup>7</sup> The ionization parameter is defined here as  $\xi = L_{\text{ion}}/n_e R^2$ , where  $L_{\text{ion}}$  is the ionizing luminosity from 1 to 1000 Ryd,  $n_e$  is the electron density, and  $R$  is the radial distance to the gas. The units of  $\xi$  are erg cm s $^{-1}$ .

<sup>8</sup> See <http://heasarc.gsfc.nasa.gov/docs/xanadu/xspec/models/reflion.html>.

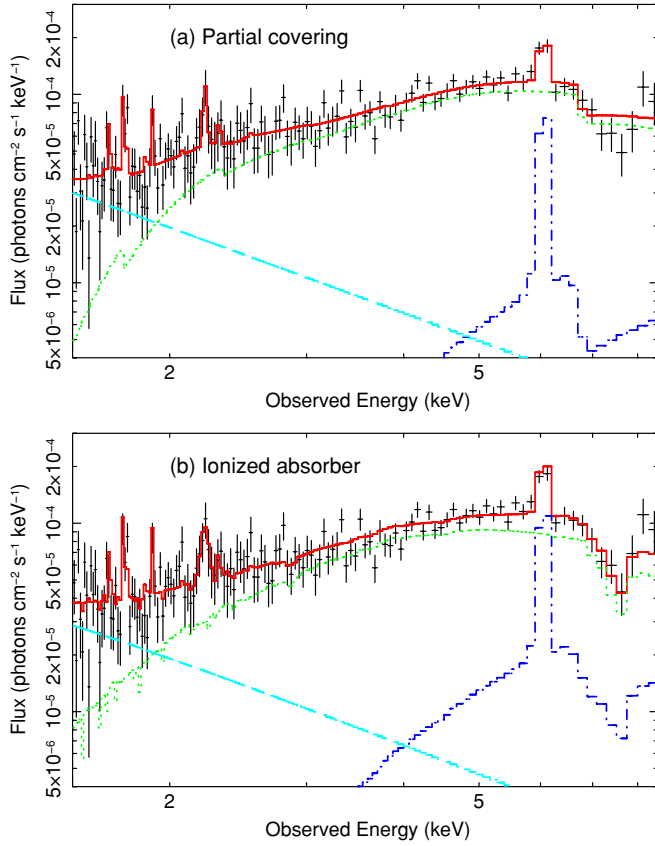


**Figure 6.** *Chandra* LETG spectrum plotted in the iron *K* band. Panel (a) shows the spectrum fitted with a neutral partial covering absorption model, as described in Section 4.2. Panel (b) shows the spectrum fitted with a partially ionized absorber, also described in Section 4.2. The solid (red) line shows the total emergent spectrum (including emission lines), the dotted (green) line the absorbed power law, the dot-dashed (blue) line the reflection component, and the dashed (cyan) line the unabsorbed scattered power law. Note that the partially ionized absorber gives a better fit in the iron *K* band.

(A color version of this figure is available in the online journal.)

Thus, crudely parameterized in this way, the edge energy is significantly greater than the *K*-shell threshold energy for neutral iron at 7.11 keV, which indicates that the iron *K* absorber toward 3C 445 may be at least partially ionized.

Thus, the neutral partially covering absorber (the model ZPCFABS in XSPEC) as well as the neutral fully covering absorber were instead replaced by a single photoionized absorber, in the form of a multiplicative grid of absorption models calculated by the XSTAR v2.1 code. The XSTAR model includes the detailed treatment of the iron *K*-shell opacity as described by Kallman et al. (2004). Solar abundances were assumed and the absorber was assumed to fully cover the line of sight to the source. Thus, the overall spectral model was in the mathematical form  $F(E) = \text{wabs} \times [\text{xstar}_{\text{abs}} \times (\text{pow1} + \text{reflionx}) + \text{pow2} + \text{xstar}_{\text{em}}]$ , where  $\text{xstar}_{\text{abs}}$  represents the multiplicative XSTAR photoionized absorber,  $\text{reflionx}$  is the Compton reflection component, and  $\text{pow1}$ ,  $\text{pow2}$ ,  $\text{xstar}_{\text{em}}$ , and  $\text{wabs}$  are the direct and scattered power laws, photoionized emitter, and neutral Galactic absorber, respectively, as described previously.

The photoionized absorption model provides an excellent fit to the LETG spectrum: the overall fit statistic is  $C/\text{dof} = 498.4/450$ , which is formally acceptable. In comparison, the fit statistic for the neutral partial covering model is somewhat worse, with  $\Delta C = +30$  for the same degrees of freedom ( $C/\text{dof} = 529.1/450$ ). Nonetheless, the partial covering model

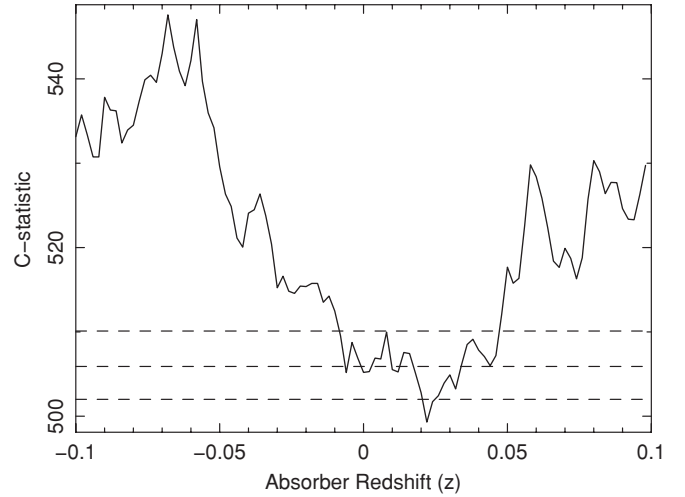


**Figure 7.** Overall fit statistic (*C*-statistic) plotted against absorber redshift (solid line). An absorber coincident with the redshift of 3C 445 at  $z = 0.056$  appears to be ruled out at  $>99.9\%$  confidence level. Note that the dashed horizontal lines represent (from bottom to top) the 90%, 99%, and 99.9% confidence levels for one interesting parameter. The best-fit absorber redshift of  $z = 0.022 \pm 0.002$  implies that the absorber has a net blueshift of  $-10,000 \text{ km s}^{-1}$  in the rest frame of 3C 445.

cannot be rejected with a high degree of certainty, as the overall fit statistic is only excluded at 90% confidence. The difference between the two absorber models is shown in Figure 6; it can be seen that the partially ionized absorber provides a better fit to the absorption in the iron *K* band and in particular the position and depth of the iron *K* absorption profile, although otherwise the fit to the data appears similar.

The parameters of the photoionized absorber model are listed in Table 3. A column density of  $N_{\text{H}} = (1.85^{+0.09}_{-0.11}) \times 10^{23} \text{ cm}^{-2}$  is found for the photoionized absorber, which is moderately ionized, with  $\log \xi = 1.42^{+0.20}_{-0.12}$ . At this ionization, iron ions in the range Fe xv–xviii are likely to dominate the spectrum (Kallman et al. 2004), although other ions may also be present. At this ionization state, the absorber consists of a blend of resonance lines from the above ions, similar to the model spectra that are shown in Figure 13 of Kallman et al. (2004), resulting in a broad absorption trough as observed in the LETG above 7 keV. Note, however, that calorimeter-based resolution in the iron *K* band would be required to resolve the absorption line structure.

Interestingly, the best-fit model appears to indicate that the absorber could be outflowing compared to the systemic velocity of 3C 445, with  $v_{\text{out}} = -(0.034 \pm 0.002)c$  (or  $v_{\text{out}} = -10200 \pm 600 \text{ km s}^{-1}$ ). Note that a solution with zero outflow velocity is excluded at  $>99.9\%$  confidence and the fit statistic is correspondingly worse by  $\Delta C = 22.3$  in this case. The apparent blueshift of the absorber is driven by the requirement to fit the absorption profile above 7 keV in the iron *K* band.

Figure 7 shows the overall fit statistic (*C*-statistic) for the absorption model, plotted against the redshift of the photoionized absorber, obtained from stepping through the absorber redshift in small increments of  $\Delta z = 10^{-3}$ . Note that all the other parameters of the absorber (e.g.,  $N_{\text{H}}$  and  $\log \xi$ ) and the continuum were also allowed to vary at each increment. Thus, an absorber at a redshift of  $z = 0.0562$  would require no net velocity shift compared to the host galaxy of 3C 445; however, an absorber redshift of  $z = 0.0562$  appears to be excluded at  $>99.99\%$  confidence from the fit statistic. Indeed the best-fit absorption model to the *Chandra* spectrum has a redshift of  $z = 0.022 \pm 0.002$ .



An intervening absorption system at an intermediate redshift of  $z = 0.022$  would appear unlikely, as this would require the whole X-ray spectrum of 3C 445 to be absorbed, rather than just the primary power law, which cannot be the case as the soft X-ray line emission is not absorbed by the  $N_H \sim 10^{23} \text{ cm}^{-2}$  column of gas. Furthermore, no intervening absorption systems are known at this redshift toward 3C 445. Thus, the most likely scenario is that the photoionized absorber in 3C 445 is outflowing, with a net blueshift of approximately  $-10,000 \text{ km s}^{-1}$  with respect to the rest frame of 3C 445.

A further, more highly ionized zone of absorbing gas is not statistically required in the LETG data; however, the *Suzaku* data may indicate the presence of such absorption at iron *K*, in the form of resonance absorption from Fe xxv or Fe xxvi (V. Braito et al. 2010, in preparation), with a similar outflow velocity to that required above. Note that the Galactic ( $z = 0$ ) absorption column is in excess of the expected value from neutral H I measurements (e.g., Dickey & Lockman 1990), which might indicate additional neutral absorption associated with the host galaxy of 3C 445.

Finally, the presence of a scattered power-law component is required in the model at high confidence ( $\Delta C = 56$ ), which is not absorbed by the high-column-density photoionized absorber. The fraction of the scattered to direct power-law emission is  $\sim 2\%$ . Thus, about 2% of the direct absorbed power law is scattered into our line of sight by free electrons in a highly ionized plasma. As we discuss below, such gas may be associated with the photoionized emission region detected in the *Chandra* spectrum.

## 5. DISCUSSION

### 5.1. The Properties of the Soft X-ray Emitting Gas

The high-resolution *Chandra* LETG observation of the BLRG 3C 445 has revealed a complex X-ray spectrum of this obscured AGN, with both emission and absorption present from layers of photoionized gas. Initially, we turn our attention to the properties of the soft X-ray line emitting gas. While the presence of the soft X-ray line emission has been detected in a previous observation with *XMM-Newton* (Sambruna et al. 2007; Grandi et al. 2007), here for the first time we detect and resolve multiple emission lines, utilizing the high spectral resolution of the *Chandra* LETG. Specifically, the *Chandra* LETG observation has resolved emission lines from highly ionized gas in the soft X-ray spectrum, primarily from the He- and H-like transitions of O, Ne, Mg, and Si, corresponding to the most abundant elements with K-shell emission lines over the 0.5–2.0 keV band. The direct detection of radiative recombination emission from O VII and O VIII also shows that the most likely origin of the soft X-ray line emission is from photoionized emission; indeed a model including emission from a collisionally ionized gas is unable to produce an acceptable fit to the spectrum.

#### 5.1.1. The Distance and Density of the Gas

The emission from the He-like triplets of O VII, Ne IX, Mg XI, and Si XIII appears to be resolved into their respective forbidden and intercombination lines. Indeed all of the He-like lines are well modeled in this manner, e.g., O VII, as discussed in Sections 3 and 4, while the line energies are in agreement with the expected rest-frame energies of the forbidden and intercombination transitions. The fact that significant intercombination emission is detected suggests that the density of the plasma is high.

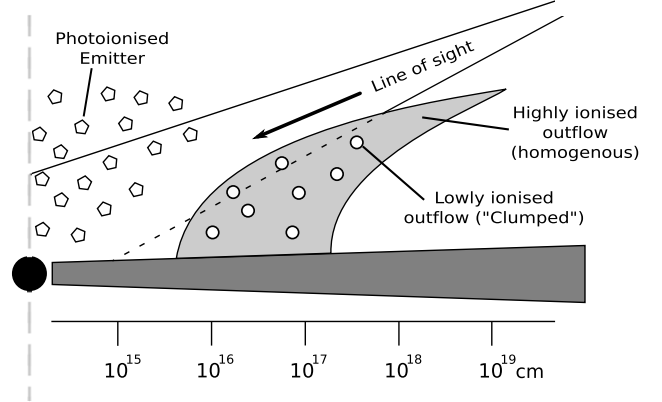


**Figure 8.** Schematic diagram showing the possible inner geometry of 3C 445. The line of sight toward the observer is represented by the solid and dashed black lines, while the gray dashed vertical line represents the direction of the radio-jet axis. In 3C 445, the line of sight toward the direct X-ray emission from the innermost region (black dashed line) is obscured by the outflowing matter, which may be in the form of a clumpy accretion disk wind. The observer has an unobscured view of the photoionized emission line clouds, which are responsible for the soft X-ray line emission. This highly ionized gas can also scatter continuum X-rays into the line of sight.

Indeed the ratio  $R$  of the forbidden to intercombination emission is close to  $R \sim 1$  (see Section 3.2.2). This sets a lower limit on the density of the He-like emitting gas of  $n_e > 10^{10} \text{ cm}^{-3}$  (see Porquet & Dubau 2000, Figure 8). Thus, an upper limit on the radial distance to the emitter from the central X-ray source can be estimated from the definition of the ionization parameter of the emitting gas, i.e.,  $R^2 = L_{\text{ion}}/\xi n_e$ . Here  $L_{\text{ion}}$  is the ionizing luminosity from 1 to 1000 Ryd, which from the best-fit continuum parameters in Table 3 gives  $L_{\text{ion}} = 3 \times 10^{44} \text{ erg s}^{-1}$  for 3C 445. The ionization parameter of the He-like emitting gas is  $\log \xi = 1.8 \text{ erg cm s}^{-1}$ , as measured from the *XSTAR* emission model (Section 4.1, Table 3), while  $n_e > 10^{10} \text{ cm}^{-3}$  as described above. Thus, the radial distance to the emitter derived from this method is  $R < 2 \times 10^{16} \text{ cm}$  (or  $< 0.01 \text{ pc}$ ). For an estimated black hole mass of 3C 445 of  $M_{\text{BH}} \sim 2 \times 10^8 M_{\odot}$  (Bettoni et al. 2003; Marchesini et al. 2004), this corresponds to a radius of  $\sim 1000 R_g$ .<sup>9</sup>

Alternatively, the location of the emitting gas can be estimated from the measured line widths of the O VII–VIII emission. The best-fit width of the three strongest emission lines (namely O VII (f) and O VIII Ly $\alpha$ ) is  $v_{\text{FWHM}} = 2600_{-600}^{+1000} \text{ km s}^{-1}$  (Section 3.2.3). Thus, assuming Keplerian motion,  $R \sim GM_{\text{BH}}/v^2$ , where we define the velocity width as  $v = \frac{\sqrt{3}}{2} v_{\text{FWHM}}$ . Thus, by this estimate  $R \sim 5 \times 10^{17} \text{ cm}$  (or  $R \sim 0.1 \text{ pc}$ ).

#### 5.1.2. The Covering Factor

We now consider the possible covering factor and column density of the emitting gas. From the *XSTAR* code,<sup>10</sup> the normalization ( $k$ ) of the line emission component (which is proportional to the flux received by the observer) is related to the global covering fraction of a quasi-spherical shell of gas by

$$k = f_{\text{cov}} L_{\text{ion}} (10^{38}) / D_{\text{kpc}}^2, \quad (1)$$

<sup>9</sup> Where  $R_g = GM/c^2$  is the gravitational radius.

<sup>10</sup> See

<http://heasarc.gsfc.nasa.gov/docs/software/xstar.docs/html/node94.html>.

**Table 3**  
Summary of LETG Model Parameters

Model Component	Fit Parameter	Value	$\Delta C$
1. Power-law continuum	$\Gamma$	$1.73^{+0.22}_{-0.19}$	
	Normalization <sup>a</sup>	$3.0 \pm 0.8 \times 10^{-3}$	
2. Scattered power law	$\Gamma$	1.73 (tied)	57.0
	Normalization <sup>a</sup>	$6.6 \pm 1.0 \times 10^{-5}$	
3. Galactic absorption	$N_{\text{H}}^{\text{Gal b}}$	$(1.5^{+0.6}_{-0.5}) \times 10^{21}$	
4. Ionized reflection	$\log \xi_{\text{refl}}^c$	$< 1.65$	96.5
	Normalization <sup>a</sup>	$(2.49^{+0.83}_{-0.62}) \times 10^{-5}$	
5. Photoionized emission	$N_{\text{H}}^b$	$10^{22f}$	125.6
	$\log \xi^c$	$1.82^{+0.13}_{-0.33}$	
	Mg abundance	$2.6^{+2.6}_{-1.5}$	
	Si abundance	$6.5^{+9.95}_{-3.86}$	
	Outflow velocity <sup>d</sup>	$+150^{+240}_{-210}$	
	Normalization <sup>e</sup> ( $k$ )	$(2.4^{+0.7}_{-0.6}) \times 10^{-6}$	
Second emission region	$\log \xi^c$	$3.0 \pm 0.4$	10.0
	Normalization <sup>e</sup> ( $k$ )	$1.2^{+1.9}_{-0.9} \times 10^{-5}$	
6. Photoionized absorber	$N_{\text{H}}^b$	$(1.85^{+0.09}_{-0.11}) \times 10^{23}$	383.5
	$\log \xi^c$	$1.42^{+0.20}_{-0.12}$	
	Blueshift	$-0.034 \pm 0.002c$	22.3
	Outflow velocity <sup>d</sup>	$-10200 \pm 600$	
7. Fit statistic	$C$	498.4/450 dof	

**Notes.**

<sup>a</sup> Normalization corresponds to flux measured at 1 keV, in units of photons  $\text{cm}^{-2} \text{s}^{-1} \text{keV}^{-1}$ .

<sup>b</sup> Column density in units of  $\text{cm}^{-2}$ .

<sup>c</sup> Ionization parameter ( $\xi$ ) in units of  $\text{erg cm s}^{-1}$ .

<sup>d</sup> Units of  $\text{km s}^{-1}$ .

<sup>e</sup> XSTAR emission normalization factor ( $k$ ) in units of  $10^{38} \text{ erg s}^{-1} \text{ kpc}^{-2}$ .

<sup>f</sup> Model parameter fixed in fit.

where  $f_{\text{cov}}$  is the global covering factor of the emitter ( $f_{\text{cov}} = 1$  for a spherical shell covering  $4\pi$  sr),  $L_{\text{ion}}(10^{38})$  is the ionizing luminosity of the source in units of  $10^{38} \text{ erg s}^{-1}$ , and  $D_{\text{kpc}}$  is the distance to 3C 445 in units of kpc. Thus, the units of  $k$  are  $10^{38} \text{ erg s}^{-1} \text{ kpc}^{-2}$ . Note that the normalization of the XSTAR emission component (or equivalently its flux) will be lower if the covering fraction of the gas is lower.

The Hubble flow distance to 3C 445 ( $z = 0.0562$ ) is  $D = 2.37 \times 10^5 \text{ kpc}$  assuming  $H_0 = 71 \text{ km s}^{-1} \text{ Mpc}^{-1}$ . From the spectral fits in Section 4 (summarized in Table 3), the normalizations of the two XSTAR emission components are  $k_{\text{low}} = 2.4 \times 10^{-6}$  for the lower-ionization gas and  $k_{\text{high}} = 1.2 \times 10^{-5}$  for the higher-ionization gas. Thus for an ionizing luminosity of  $3 \times 10^{44} \text{ erg s}^{-1}$ , the covering fractions of the low- and high-ionization emission regions are 0.045 and 0.22, respectively.

Note that this calculation is for a column density of  $N_{\text{H}} = 10^{22} \text{ cm}^{-2}$  for the emitter, which has been assumed in the XSTAR model. For the emitter, the column density and covering factor are largely degenerate upon each other: in other words, if a lower column is assumed then the covering fraction of the gas will need to be correspondingly higher to compensate in order to reproduce the same observed emission line spectrum. Nonetheless, the covering fraction cannot be  $f_{\text{cov}} > 1$  and hence a lower limit to the column density of  $N_{\text{H}} > 2.2 \times 10^{21} \text{ cm}^{-2}$  is derived for the high-ionization gas.

For a plausible upper limit to the column density of the emitting gas, one may consider the fraction of the observed X-ray power-law continuum that is electron scattered into our line of sight. From the best-fit model listed in Table 3, the ratio

of the scattered to directly observed continuum is 0.02. Note that the presence of such a scattered component is required by the data at a high confidence level. Thus, the fraction of scattered photons is equivalent to  $1 - \exp(-\sigma_{\text{T}} N_{\text{H}}) = 0.02$ , where  $\sigma_{\text{T}} = 6.65 \times 10^{-25} \text{ cm}^2$  is the Thomson cross section. Hence the column required to reproduce the scattered power-law emission is  $N_{\text{H}} = 3 \times 10^{22} \text{ cm}^{-2}$ . Note that this electron scattering zone may be associated with the highest-ionization gas in the emission line region (which may be more extended than the lower-ionization region), which scatters the primary X-ray continuum back into our line of sight. Such gas is indeed envisaged in AGN Unification scenarios (Antonucci 1993) and may be responsible for the broad, permitted lines seen in polarized light in the optical spectra of type-2 AGNs.

The approximate mass of the emitting gas can also be estimated. The total mass of the emitter is equal to  $M = 1.23 f_{\text{cov}} \times 4\pi R^2 N_{\text{H}} m_{\text{p}}$ , where the factor of 1.23 arises from the solar composition of the gas. We adopt the radius of the emitting gas derived in Section 5.1.1 from the He-like triplets of  $R \sim 0.01 \text{ pc}$ . From the possible range of column densities discussed above of  $N_{\text{H}} = (2 \times 10^{21} - 3 \times 10^{22}) \text{ cm}^{-2}$ , corresponding to covering fractions of between  $f_{\text{cov}} = 1.0$  and  $0.08$ , respectively, then the emitter mass is only  $M \sim 0.03 M_{\odot}$ . However, the mass will be considerably higher for larger  $R$ , i.e., if the larger radius of  $R \sim 0.1 \text{ pc}$  is adopted from the Keplerian width of the oxygen lines (see Section 5.1.1), then the mass will be of the order  $M \sim 3 M_{\odot}$ .

### 5.1.3. Emission from an X-ray Broad-line Region?

Thus, the possible radius derived for emitting gas of  $R \sim 0.01$ – $0.1 \text{ pc}$  appears to be well inside the expected radii for the NLR (i.e., pc to kpc scales) and also within the expected size scale of a putative parsec-scale molecular torus. Furthermore the likely density of this gas, of  $n_{\text{e}} \sim 10^{10} \text{ cm}^{-3}$ , appears much higher than what one would associate with typical NLR densities (e.g.,  $n_{\text{e}} \sim 10^3 \text{ cm}^{-3}$ ; Koski 1978).

Instead the range of radii and densities calculated above appears to be consistent with what is typically expected in the AGN BLR of Seyfert 1 galaxies and quasars (e.g., Wandel et al. 1999; Kaspi et al. 2000; Peterson et al. 2004). Indeed the velocity width measured here of  $\sim 2600 \text{ km s}^{-1}$  (FWHM) is similar to the measured H $\alpha$  FWHM width for 3C 445 of  $6400 \text{ km s}^{-1}$  (Eracleous & Halpern 1994) or the H $\beta$  FWHM of  $3000 \text{ km s}^{-1}$  (Osterbrock et al. 1976).

Recently, broadened soft X-ray lines were detected by Longinotti et al. (2008) during an *XMM-Newton* RGS observation of the Seyfert 1 Mrk 335 during a low flux state. The O VIII Ly $\alpha$  line was resolved with a FWHM width of  $2200 \pm 750 \text{ km s}^{-1}$ , consistent with the H $\beta$  width of this Seyfert 1 (Boroson & Green 1992). From photoionization arguments, Longinotti et al. (2008) placed a limit on the radial distance to the soft X-ray emitting gas of  $< 0.06 \text{ pc}$ , consistent with a BLR origin. A similar claim has been made by Blustin & Fabian (2009), who detected several broadened soft X-ray emission lines with a typical FWHM of  $\sim 5000 \text{ km s}^{-1}$  from a deep *XMM-Newton* RGS observation of the narrow-line Seyfert 1, 1H 0707-495. Indeed there have also been several past claims of broadened soft X-ray emission lines from grating observations of Seyfert 1s, with line widths which appear to be consistent with a BLR origin (e.g., NGC 4051, Ogle et al. 2004; NGC 5548, Steenbrugge et al. 2005; Mrk 509, Smith et al. 2007; Mrk 279, Costantini et al. 2007). Thus, we may be observing the same X-ray BLR emission in the BLRG 3C 445.

### 5.2. Absorption from an Accretion Disk Wind in 3C 445?

As has also been found from previous observations (Sambruna et al. 2007; Grandi et al. 2007), the primary X-ray continuum from 3C 445 is highly absorbed, with a column density exceeding  $10^{23} \text{ cm}^{-2}$ . Indeed the X-ray column observed toward 3C 445 far exceeds the expected column based on the extinction in the optical band toward this AGN, of the order  $E_{B-V} \sim 1$  (Rudy & Tokunaga 1982). Although the properties of the absorbing gas were unclear from previous shorter (and lower spectral resolution) observations, the *Chandra* LETG shows that the absorption can be well modeled with a moderately ionized outflow, with an outflow velocity of the order  $\sim 10,000 \text{ km s}^{-1}$ . As we will discuss here, it appears more plausible that this absorbing gas is associated with a disk wind on smaller (sub-parsec) scales rather than with a putative molecular torus.

#### 5.2.1. The Likely Location of the Wind

We first consider the location of the absorber. For a homogeneous radial wind, the observed column density along the line of sight is equal to

$$N_H = \int_{R_{\text{in}}}^{R_{\text{out}}} n_e(R) dR = \int_{R_{\text{in}}}^{R_{\text{out}}} \frac{L_{\text{ion}}}{\xi R^2} dR = \frac{L_{\text{ion}}}{\xi} \left( \frac{1}{R_{\text{in}}} - \frac{1}{R_{\text{out}}} \right), \quad (2)$$

where  $R_{\text{in}}$  and  $R_{\text{out}}$  are the inner and outer radii along the line of sight through the wind. In the case where we are looking directly down a homogeneous wind toward an inner radius  $R_{\text{in}}$ , then  $R_{\text{out}} = \infty$  and re-arranging gives  $R_{\text{in}} = L_{\text{ion}}/\xi N_H$ . The best-fit XSTAR model of the absorber (Table 3) gives  $N_H = 2 \times 10^{23} \text{ cm}^{-2}$  and  $\log \xi = 1.4$ ; thus  $R_{\text{in}} = 5 \times 10^{19} \text{ cm}$  (or  $\sim 10 \text{ pc}$ ). At this radius, the density of the absorbing matter is  $n_e \sim 10^4 \text{ cm}^{-3}$ .

Thus, a radius of  $\sim 10 \text{ pc}$  is consistent with a wind launched from the region of the molecular torus. However, this can be considered an upper limit if we are only viewing across the wind, or if the wind is sufficiently clumpy, as we will argue in Section 5.3 from considering the wind energetics. In this case, we can define the wind thickness as  $\Delta R = R_{\text{out}} - R_{\text{in}}$  and assuming  $\Delta R/R \ll 1$ , then re-arranging Equation (2) gives

$$R_{\text{in}} = \frac{L_{\text{ion}}}{\xi N_H} \left( \frac{\Delta R}{R} \right). \quad (3)$$

So if  $\Delta R/R \ll 1$  then the wind can originate on much more compact scales. Indeed if the location of the X-ray absorber is on parsec scales, then this presents a problem for both the soft X-ray emission line gas and the emission from the optical BLR. Thus, the location of the absorber cannot be outside the soft X-ray line emission region, as otherwise the emission lines would be completely obscured. This is certainly not the case from the LETG spectrum, i.e., the soft X-ray emission is absorbed by a much lower column density of  $N_H = 1.5 \times 10^{21} \text{ cm}^{-2}$  (see Table 3). Furthermore, the emission from the optical BLR in 3C 445 cannot be strongly obscured by the X-ray absorbing gas, given its classification as a BLRG and the observation of broad permitted lines such as  $H\alpha$  or  $H\beta$  in non-polarized light (Eracleous & Halpern 1994). Thus, the observational evidence suggests a more compact size-scale for the X-ray absorber in 3C 445 than the parsec-scale torus.

For a scenario whereby the absorber originates from a wind launched off the accretion disk by radiation pressure, we can calculate a lower bound on the launch radius from the escape

velocity. The escape radius is  $R_{\text{esc}} = 2c^2 R_g / v_{\text{out}}^2$ , where  $R_g = 3 \times 10^{13} \text{ cm}$  (for  $M_{\text{BH}} = 2 \times 10^8 M_\odot$ ) and  $v_{\text{out}} = 10^4 \text{ km s}^{-1}$ . Thus for the outflow in 3C 445,  $R_{\text{esc}} \sim 3 \times 10^{16} \text{ cm}$  (or  $\sim 0.01 \text{ pc}$ ). This would appear to be a more plausible radius at which the wind is viewed, as while the central X-ray continuum would be absorbed, the sight line toward the soft X-ray emission need not be obscured. At this radius the density would be higher,  $n_e \sim 10^{10} \text{ cm}^{-3}$ , while the gas will be substantially clumped, i.e.,  $\Delta R/R \sim 10^{-3}$ .

Indeed such a scenario could also be consistent with the absorbing clumps or clouds partially covering the line of sight to the central X-ray emitter. In this scenario, in order for the clouds to only partially obscure the primary X-ray continuum, they would likely have to be only a few gravitational radii in size, i.e., of the order  $\sim 10^{14} \text{ cm}$ . If the column density through an individual cloud is  $N_H \sim 10^{23} \text{ cm}^{-2}$ , this would require a density of  $n \sim 10^9 \text{ cm}^{-3}$ . Given an observed ionization parameter of  $\log \xi = 1.4$ , this then implies a radial distance to the clouds of  $\sim 10^{17} \text{ cm}$ , i.e., consistent with a sub-parsec-scale location.

#### 5.3. The Wind Energetics

For a quasi-spherical radial outflow, the mass outflow rate is given by

$$\dot{M}_{\text{out}} = 1.23 \times 4\pi b R^2 n_e m_p v_{\text{out}} = 1.23 \times 4\pi b \left( \frac{L_{\text{ion}}}{\xi} \right) m_p v_{\text{out}}, \quad (4)$$

where for the absorber in 3C 445,  $L_{\text{ion}}/\xi = 10^{43} \text{ cm}^{-1}$ , while  $b$  is a geometrical factor:  $b = 1$  for a homogeneous spherical outflow, but  $b < 1$  for a wind covering a fraction of  $4\pi \text{ sr}$  or if the matter is clumped. Thus for the absorber in 3C 445, then  $\dot{M}_{\text{out}} = 2.5b \times 10^{29} \text{ g s}^{-1}$  or  $\dot{M}_{\text{out}} = 4000b M_\odot \text{ yr}^{-1}$ . This seems implausibly high for  $b = 1$ .

For comparison, we can estimate the likely accretion rate needed to power the bolometric (radiative) output of 3C 445. The (unabsorbed) 2–10 keV X-ray luminosity of 3C 445 is  $L_{2-10} = 1 \times 10^{44} \text{ erg s}^{-1}$  and assuming the 2–10 keV luminosity is approximately 5% of the bolometric output (e.g., Elvis et al. 1994), then  $L_{\text{bol}} = 2 \times 10^{45} \text{ erg s}^{-1}$ , also in agreement with the estimate of Marchesini et al. (2004). For an accretion efficiency of  $\eta = 0.05$ , the accretion rate is then  $\dot{M}_{\text{acc}} = L_{\text{bol}}/\eta c^2 \sim 1 M_\odot \text{ yr}^{-1}$  for 3C 445. Thus, a homogeneous wind requires  $\dot{M}_{\text{out}} \gg \dot{M}_{\text{acc}}$  for 3C 445, which would rather rapidly exhaust the supply of gas toward the central AGN.

Instead we consider the outward transfer of momentum into the wind via radiation pressure. Thus, the outward momentum rate is  $\dot{p} = \dot{M}_{\text{out}} v_{\text{out}} = L_{\text{bol}}/c \sim 10^{35} \text{ g cm s}^{-2}$ . For the measured outflow velocity  $v_{\text{out}} = 10^9 \text{ cm s}^{-1}$ , then the mass outflow rate is  $\dot{M}_{\text{out}} \sim 10^{26} \text{ g s}^{-1}$  (or  $\sim 1 M_\odot \text{ yr}^{-1}$ ). This appears more physically realistic with  $\dot{M}_{\text{out}} \sim \dot{M}_{\text{acc}}$  and requires a clumping factor of  $b \sim 10^{-3}$ , which may be the case if the absorbing clouds are located on sub-parsec scales as discussed above. Furthermore, we note that the *Suzaku* spectrum of 3C 445 (V. Braito et al. 2010, in preparation) may require a very high ionization zone ( $\log \xi \sim 4$ ) of absorbing gas in addition to the moderately ionized absorber discussed here. Indeed both the low- and high-ionization absorption may co-exist at the same radii in a multi-phase disk-wind, with the low-ionization absorber present as higher-density clouds confined within the lower-density and more uniform high-ionization outflow (see Figure 8).

Finally, we estimate the total mechanical output of the wind in 3C 445. The kinetic power is simply  $\dot{E} = \dot{M}_{\text{out}} v_{\text{out}}^2 / 2 \sim$



$10^{47} b \text{ erg s}^{-1}$ , which for  $b \sim 10^{-3}$ , as discussed above, implies  $\dot{E} \sim 10^{44} \text{ erg s}^{-1}$ , which is approximately 10% of  $L_{\text{bol}}$ . Note that the presence of a high-ionization outflow of  $\log \xi \sim 4$ , as implied by the *Suzaku* data, also suggests a similar mechanical output, but without the requirement that the absorbing gas is clumped.

#### 5.4. The Overall Geometry of 3C 445

Given the likely high inclination of 3C 445 compared to the radio-jet axis, of the order  $60^\circ$ – $70^\circ$  (Leahy et al. 1997; Eracleous & Halpern 1998), it is plausible that we are viewing the central engine of 3C 445 at a relatively side-on orientation. The situation may be similar to that outlined in Figure 8. Thus, we may be viewing through an equatorial disk-wind in 3C 445, on scales of approximately  $10^{16}$ – $10^{17}$  cm from the central black hole. In this toy model for 3C 445, the soft X-ray emitting clouds may be lifted above the plane of the accretion disk and could be associated with the optical BLR emission, as discussed earlier. Any highly ionized gas that is present would also serve to Thomson scatter the primary absorbed X-ray continuum back into our line of sight, as is also observed in the *Chandra* spectrum.

The lower-ionization absorbing gas viewed here might be clumped, within a much higher-ionization, but lower-density medium, co-existing at a similar radius to the high-ionization gas. If such high column density ( $\sim 10^{23} \text{ cm}^{-2}$ ) but low-ionization absorbing gas were located on much larger scales, e.g., with a parsec-scale torus, it would be difficult to reconcile the high column density with the much lower absorbing column (of  $N_{\text{H}} \sim 10^{21} \text{ cm}^{-2}$ ), toward the soft X-ray line emitting gas, if the latter is coincident with sub-parsec-BLR scales. Instead the much lower column density gas which absorbs the soft X-ray emission spectrum might instead be associated with gas on the scale of the host galaxy and would be consistent with the amount of reddening observed toward 3C 445 (Rudy & Tokunaga 1982).

Finally, if the high column absorbing medium is clumped, it might be possible to observe short-timescale  $N_{\text{H}}$  variability, due to the passage of clouds along our line of sight. For instance, such absorption variability is observed along the line of sight to some Seyfert galaxies, the most notable example being the intermediate-type Seyfert, NGC 1365 (Risaliti et al. 2009; Maiolino et al. 2010). However, no such column density variations have been apparent so far toward 3C 445, either on short timescales within the 200 ks *Chandra* observations or on longer timescales, as the total column density is also consistent with previous observations, e.g., with *XMM-Newton* (Sambruna et al. 2007; Grandi et al. 2007). However, this may simply be explained if the number of absorbing clouds is large, which would average out any variations.

## 6. CONCLUSIONS

We have reported on a deep 200 ks *Chandra* LETG spectrum of the absorbed BLRG, 3C 445, which displays a complex X-ray spectrum. The high-resolution *Chandra* spectrum revealed a wealth of soft X-ray emission lines from a photoionized plasma, primarily from the He- and H-like transitions of O, Ne, Mg, and Si. The O VII and O VIII lines are resolved, with a typical FWHM width of  $\sim 2600 \text{ km s}^{-1}$ , while the ratio of forbidden to intercombination emission in the He-like triplets indicates a high electron density of  $n_e > 10^{10} \text{ cm}^{-3}$  (Porquet & Dubau 2000). Thus, the X-ray lines appear to be consistent with an origin in the optical BLR in 3C 445, located on sub-parsec scales.

The *Chandra* spectrum of 3C 445 is also highly absorbed and can be modeled either by partially covering or by partially ionized absorbing gas. The high-column-density gas may be associated with an equatorial accretion disk wind in 3C 445, observed at high inclinations with respect to the radio-jet axis. Future high-resolution observations of 3C 445, with calorimeter resolution in the iron *K* band, e.g., with *Astro-H*, will potentially resolve a host of absorption lines associated with the high-column-density absorber, enabling us to probe the kinematics of any outflowing wind to a high level of accuracy.

This research has made use of data obtained from the High Energy Astrophysics Science Archive Research Center (HEASARC), provided by NASA's Goddard Space Flight Center. R.S. acknowledges support from NASA through the *Suzaku* and *Chandra* programs. We also thank Tahir Yaqoob for assistance with the *Chandra* data analysis.

## REFERENCES

- Anders, E., & Grevesse, N. 1989, *Geochim. Cosmochim. Acta*, **53**, 197
- Antonucci, R. 1993, *ARA&A*, **31**, 473
- Bettoni, D., Falomo, R., Fasano, G., & Govoni, F. 2003, *A&A*, **399**, 869
- Blandford, R. D., & Payne, D. G. 1982, *MNRAS*, **199**, 883
- Blustin, A. J., & Fabian, A. C. 2009, *MNRAS*, **399**, L169
- Blustin, A. J., Page, M. J., Fuerst, S. V., Branduardi-Raymont, G., & Ashton, C. E. 2005, *A&A*, **431**, 111
- Boroson, T. A., & Green, R. F. 1992, *ApJS*, **80**, 109
- Brinkman, A. C., et al. 2000, *ApJ*, **530**, L111
- Cash, W. 1979, *ApJ*, **228**, 939
- Corbett, E. A., Robinson, A., Axon, D. J., Young, S., & Hough, J. H. 1998, *MNRAS*, **296**, 721
- Costantini, E., et al. 2007, *A&A*, **461**, 121
- Crenshaw, D. M., Kraemer, S. B., & George, I. M. 2003, *ARA&A*, **41**, 117
- Crenshaw, D. M., Peterson, B. M., & Wagner, R. M. 1988, *AJ*, **96**, 1208
- Dickey, J. M., & Lockman, F. J. 1990, *ARA&A*, **28**, 215
- Elvis, M., et al. 1994, *ApJS*, **95**, 1
- Eracleous, M., & Halpern, J. P. 1994, *ApJS*, **90**, 1
- Eracleous, M., & Halpern, J. P. 1998, *ApJ*, **505**, 577
- Eracleous, M., & Halpern, J. P. 2004, *ApJS*, **150**, 181
- Gallagher, S. C., & Everett, J. E. 2007, in ASP Conf. Ser. 373, The Central Engine of Active Galactic Nuclei, ed. L. C. Ho & J.-M. Wang (San Francisco, CA: ASP), 305
- Grandi, P., Guainazzi, M., Cappi, M., & Ponti, G. 2007, *MNRAS*, **381**, 21
- Grandi, P., Malaguti, G., & Focci, M. 2006, *ApJ*, **642**, 113
- Grevesse, N., & Sauval, A. J. 1998, *Space Sci. Rev.*, **85**, 161
- Guainazzi, M., & Bianchi, S. 2007, *MNRAS*, **374**, 1290
- Hewitt, A., & Burbidge, G. 1991, *ApJS*, **75**, 297
- Kaastra, J. S., & Mewe, R. 1993, *A&AS*, **97**, 443
- Kallman, T. R., & McCray, R. 1982, *ApJS*, **50**, 263
- Kallman, T. R., Palmeri, P., Bautista, M. A., Mendoza, C., & Krolik, J. H. 2004, *ApJS*, **155**, 675
- Kaspi, S., Smith, P. S., Netzer, H., Maoz, D., Jannuzi, B. T., & Giveon, U. 2000, *ApJ*, **533**, 631
- Kataoka, J., et al. 2007, *PASJ*, **59**, 279
- Kinkhabwala, A., et al. 2002, *ApJ*, **575**, 732
- Königl, A., & Kartje, J. A. 1994, *ApJ*, **434**, 446
- Koski, A. 1978, *ApJ*, **223**, 56
- Kronberg, P. P., Wielebinski, R., & Graham, D. A. 1986, *A&A*, **169**, 63
- Leahy, J. P., Black, A. R. S., Dennett-Thorpe, J., Hardcastle, M. J., Komisarov, S., Perley, R. A., Riley, J. M., & Scheuer, P. A. G. 1997, *MNRAS*, **291**, 20
- Longinotti, A. L., Nucita, A., Santos-Lleo, M., & Guainazzi, M. 2008, *A&A*, **484**, 311
- Maiolino, R., et al. 2010, *A&A*, **517**, 47
- Marchesini, D., Celotti, A., & Ferrarese, L. 2004, *MNRAS*, **351**, 733
- McKernan, B., Yaqoob, T., & Reynolds, C. S. 2007, *ApJ*, **379**, 1359
- McKinney, J. C. 2006, *MNRAS*, **368**, 1561
- Morganti, R., Killen, N. E. B., & Tadhunter, C. N. 1993, *MNRAS*, **263**, 1023
- Morrison, R., & McCammon, D. 1983, *ApJ*, **270**, 119
- Ogle, P. M., Mason, K. O., Page, M. J., Salvi, N. J., Cordova, F. A., McHardy, I. M., & Priedhorsky, W. C. 2004, *ApJ*, **606**, 151
- Osterbrock, D. E., Koski, A. T., & Phillips, M. M. 1976, *ApJ*, **206**, 898
- Peterson, B. M., et al. 2004, *ApJ*, **613**, 682



- Piconcelli, E., Bianchi, S., Miniutti, G., Fiore, F., Guainazzi, M., Jimenez-Bailon, E., & Matt, G. 2008, [A&A](#), **480**, 671
- Porquet, D., & Dubau, J. 2000, [A&AS](#), **143**, 495
- Pounds, K. A. 1990, *MNRAS*, **242**, 20
- Reeves, J. N., Sambruna, R. M., Braitto, V., & Eracleous, M. 2009, [ApJ](#), **702**, L187
- Reeves, J. N., & Turner, M. J. L. 2000, [MNRAS](#), **316**, 234
- Reynolds, C. S. 1997, *MNRAS*, **286**, 513
- Risaliti, G., et al. 2009, [MNRAS](#), **393**, L1
- Ross, R. R., & Fabian, A. C. 2005, [MNRAS](#), **358**, 211
- Ross, R. R., Fabian, A. C., & Young, A. J. 1999, [MNRAS](#), **306**, 461
- Rudy, R. J., & Tokunaga, A. T. 1982, [ApJ](#), **256**, L1
- Sambruna, R. M., Eracleous, M., & Mushotzky, R. F. 1999, [ApJ](#), **526**, 60
- Sambruna, R. M., George, I. M., Mushotzky, R. F., Nandra, K., & Turner, T. J. 1998, [ApJ](#), **495**, 749
- Sambruna, R. M., Reeves, J. N., & Braitto, V. 2007, [ApJ](#), **665**, 1030
- Sambruna, R. M., et al. 2009, [ApJ](#), **700**, 1473
- Smith, R. A. N., Page, M. J., & Branduardi-Raymont, G. 2007, [A&A](#), **461**, 135
- Smith, R. K., Brickhouse, N. S., Liedahl, D. A., & Raymond, J. C. 2001, [ApJ](#), **556**, L91
- Spergel, D. N., et al. 2003, [ApJS](#), **148**, 175
- Steenbrugge, K. C., et al. 2005, [A&A](#), **434**, 569
- Tombesi, F., Cappi, M., Reeves, J. N., Palumbo, G. G. C., Yaqoob, T., Braitto, V., & Dadina, M. 2010a, [A&A](#), **521**, 57
- Tombesi, F., Sambruna, R., Reeves, J. N., Braitto, V., Ballo, L., Gofford, J., Cappi, M., & Mushotzky, R. 2010b, [ApJ](#), **719**, 700
- Torresi, E., Grandi, P., Guainazzi, M., Palumbo, G. G. C., Ponti, G., & Bianchi, S. 2009, [A&A](#), **498**, 61
- Torresi, E., Grandi, P., Longinotti, A., Guainazzi, M., Palumbo, G. G. C., Tombesi, F., & Nucita, A. 2010, *MNRAS*, **401**, 10
- Tueller, J., et al. 2010, [ApJS](#), **186**, 378
- Turner, T. J., George, I. M., Nandra, K., & Mushotzky, R. F. 1997, [ApJ](#), **488**, 164
- Turner, T. J., & Miller, L. 2009, *A&AR*, **17**, 47
- Turner, T. J., & Pounds, K. A. 1989, *MNRAS*, **240**, 833
- Urry, M., & Padovani, P. 1995, *PASP*, **107**, 903
- Wandel, A., Peterson, B. M., & Malkan, M. A. 1999, [ApJ](#), **526**, 579